Rayleigh-Bénard convection in a homeotropically aligned nematic liquid crystal

Leif Thomas,[1] Werner Pesch,[2] and Guenter Ahlers[1]
[1]*Department of Physics and Center for Nonlinear Science, University of California at Santa Barbara, Santa Barbara, California 93106*
[2]*Institut für Theoretische Physik, Universität Bayreuth, Bayreuth, Germany*
(Received 22 April 1998)

We report experimental results for convection near onset in a thin layer of a homeotropically aligned nematic liquid crystal heated from below as a function of the temperature difference ΔT and the applied vertical magnetic field H. When possible, these results are compared with theoretical calculations. The experiments were done with three cylindrical cells of aspect ratios [(radius)/(height)] $\Gamma = 10.6$, 6.2, and 5.0 over the field range $8 \lesssim h \equiv H/H_F \lesssim 80$ ($H_F = 20.9$, 12.6, and 9.3 G are the Fréedericksz fields for the three cells). We used the Nusselt number $\mathcal{N}$ (effective thermal conductivity) to determine the critical Rayleigh number R_c and the nature of the transition. We analyzed digital images of the flow patterns to study the dynamics and to determine the mean wave numbers of the convecting states. For h less than a codimension-two field $h_{ct} \simeq 46$ the bifurcation is subcritical and oscillatory, with traveling- and standing-wave transients. Beyond h_{ct} the bifurcation is stationary and subcritical until a tricritical field $h_t = 57.2$ is reached, beyond which it is supercritical. We analyzed the patterns to obtain the critical wave number k_c and, for $h < h_{ct}$, the Hopf frequency ω_c. In the subcritical range we used the early transients towards the finite-amplitude state for this purpose. The bifurcation sequence as a function of h found in the experiment confirms the qualitative aspects of the theoretical predictions. Even quantitatively the measurements of R_c, k_c, and Ω_c are reproduced surprisingly well considering the complexity of the system. However, the value of h_{ct} is about 10% higher than the predicted value and the results for k_c are systematically below the theory by about 2% at small h and by as much as 7% near h_{ct}. At h_{ct}, k_c is continuous within the experimental resolution whereas the theory indicates a 7% discontinuity. The theoretical tricritical field $h_t^{th} = 51$ is somewhat below the experimental one. The fully developed flow above R_c for $h < h_{ct}$ has a very slow chaotic time dependence that is unrelated to the Hopf frequency. For $h_{ct} < h < h_t$ the subcritical stationary bifurcation also leads to a chaotic state. The chaotic states persist upon reducing the Rayleigh number below R_c, i.e., the bifurcation is hysteretic. Above the tricritical field h_t, we find a bifurcation to a time independent pattern which within our resolution is nonhysteretic. However, in this field range, there is a secondary hysteretic bifurcation that again leads to a chaotic state observable even slightly below R_c. We discuss the behavior of the system in the high-field limit, and show that at the largest experimental field values R_c and k_c are within 6% and 1%, respectively, of their values for an infinite field. [S1063-651X(98)00511-X]

PACS number(s): 61.30.−v, 47.54.+r, 47.20Bp

I. INTRODUCTION

Convection in a thin horizontal layer of an isotropic fluid heated from below by a heat current $\vec{Q}$ is well known as Rayleigh-Bénard convection (RBC) [1,2]. When the fluid is a nematic liquid crystal (NLC), this phenomenon is altered in interesting ways [3]. NLC molecules are long, rodlike objects that are orientationally ordered relative to their neighbors, but whose centers of mass have no positional order [4,5]. The axis parallel to the average orientation is called the director $\hat{n}$. By confining the NLC between two properly treated parallel plates [6], one can obtain a sample with uniform planar (parallel to the surfaces, i.e., in the x-y plane) or homeotropic (perpendicular to the surfaces, or parallel to the z-axis) alignment of $\hat{n}$. The alignment can be reinforced by the application of a magnetic field $\vec{H}$ parallel to the intended direction of $\hat{n}$. This is so because the diamagnetic susceptibility is anisotropic, usually being larger in the direction parallel to the long axis of the molecules. The phenomena that occur near the onset of convection depend on the orientation of $\hat{n}$ and $\vec{H}$ [3]. In this paper we are concerned with a horizontal layer of a *homeotropically* aligned NLC in a vertical magnetic field ($\vec{H} = H\hat{e}_z$) and heated from below. In that case, $\vec{Q} = Q\hat{e}_z$ is parallel to $\hat{n}$ when the system is in the conduction state. At a critical temperature difference $\Delta T_c(H)$ the fluid will undergo a transition from conduction to convection. The precise value of $\Delta T_c(H)$, the nature of the bifurcation at $\Delta T_c(H)$, and the pattern-formation phenomena beyond $\Delta T_c(H)$ are expected to depend in interesting ways upon H [7–10].

A feature common to the homeotropic NLC and to an isotropic fluid heated from below is that the system is isotropic in the horizontal plane. Thus the convection pattern may form with no preference being given to a particular horizontal axis unless the experimental apparatus introduces an asymmetry. In both cases, the convection is driven by the buoyancy force. However, the mechanism in the NLC case is more involved [7–9]. The usual destabilization due to the thermally induced density gradient is opposed by the stiffness of the director field, which is coupled to and distorted by any flow. Since relaxation times of the director field are much longer than thermal relaxation times, it is possible for

director fluctuations and temperature or velocity fluctuations to be out of phase as they grow in amplitude. The existence of two very different time scales and this phase shift typically lead to an oscillatory instability (also known as overstability), i.e., the bifurcation at which these time-periodic perturbations acquire a positive growth rate is a Hopf bifurcation [7,8,11]. This case is closely analogous to convection in binary-fluid mixtures with a negative separation ratio [12,13]. In that case, concentration gradients oppose convection, and concentration diffusion has the slow and heat diffusion the fast time scale. As in the binary mixtures, the Hopf bifurcation in the NLC case is subcritical [9,10]. For the NLC the fully developed nonlinear state no longer is time periodic. Instead, the statistically stationary state above the bifurcation is one of spatiotemporal chaos with a typical time scale that is about two orders of magnitude slower than the theoretical inverse Hopf frequency [14]. However, it is possible to actually measure the Hopf frequency by looking at the growth or decay of small perturbations that are either deliberately introduced [9] or that occur spontaneously when the system is close to the conduction state and near the bifurcation point.

A linear stability analysis of this system was carried out by several investigators [8,15–17]. A very detailed analysis was presented by Feng, Decker, Pesch, and Kramer (FDPK) [10]. These authors also provided a weakly nonlinear analysis, which allowed the distinction between subcritical and supercritical bifurcations. Quantitative bifurcation diagrams were predicted for the nematic liquid crystal MBBA [N-(p-methodxylbenzylidine)-p-butylaniline]. In the present work we repeated and slightly extended the calculations for the material 5CB (4-n-pentyl-4'-cyanobiphenyl) (see below) used in our experiments. Since the material parameters of MBBA and 5CB are similar, we found qualitatively the same bifurcation sequences as a function of the field. Here we outline briefly the theoretical results and their relationship to our experimental results.

As the magnetic field is increased, a subcritical Hopf bifurcation line is expected to terminate at H_{ct} in a codimension-two point (CTP) beyond that the perturbations which first acquire a positive growth rate are at zero frequency. Close to but beyond the CTP this stationary bifurcation is predicted to also be subcritical. At an even higher field H_t a tricritical point (TCP) is predicted to exist beyond which the primary bifurcation is expected to become supercritical. To our knowledge there are no predictions about the patterns that should form beyond either the subcritical Hopf bifurcation below the CTP or the subcritical stationary bifurcation between the CTP and the TCP. Although there are no explicit predictions of the patterns for $H>H_t$, in analogy to isotropic fluids one might expect convection rolls above the supercritical bifurcation, unless non-Boussinesq effects [18,19] yield a transcritical bifurcation to hexagons.

The phenomena described above were previously explored only partially by experiment. Except for recent measurements at relatively small fields [14], the experiments have been qualitative or semiquantitative [9,20]. In the present paper we report the results of an extensive sytematic experimental investigation of this system, which covered a wide range of magnetic fields H. In agreement with previous work [9,20], we find a subcritical Hopf bifurcation at relatively small H that terminates in a codimension-two point (CTP). The CTP is located at a slightly higher field than the theoretical prediction. We measured the Hopf frequency $\omega_c(H)$ from visualizations of the spontaneous small-amplitude early transients just above ΔT_c. Except for the influence of the small shift of the CTP, we found $\omega_c(H)$ to be in quantitative agreement with the theory. From these transients, we also determined the critical wave vector $k_c(H)$, and found it to be typically a few percent smaller than the theoretical value. The reason for this small difference between theory and experiment is not known. As reported previously [14], we found the convecting nonlinear state for ΔT above ΔT_c to be one of spatiotemporal chaos (STC). Except at very small H, its characteristic wave number was smaller than k_c and insensitive to H and ΔT. A long-time average of the structure factor of this state was consistent with the expected rotational invariance of the system. Depending on H, the lower limit ΔT_s at which this chaotic state made its hysteretic transition back to the conduction state was found to be 10 to 25% below $R_c(H)$. The convective heat transport was consistent with that of an isotropic fluid with an average conductivity given by $\lambda_{\mathrm{avg}}=(2\lambda_\perp+\lambda_\parallel)/3$ where $\lambda_\perp$ and $\lambda_\parallel$ are the conductivities perpendicular and parallel to $\hat{n}$, respectively. This suggests a thorough randomization of the director orientations by the flow.

Beyond the CTP we found a subcritical stationary bifurcation, as had been predicted [10]. The finite-amplitude state that evolved was also a state of STC, but beyond a certain field value greater than H_{ct} it had distinctly different properties from the chaotic state at lower H. This difference was clearly evident from a discontinuity (as a function of H) of the characteristic wave number of the nonlinear state, which was larger at the larger fields. There is no theoretical guidance for the interpretation of these experimentally observed phenomena.

The range $H\geqslant H_t$ was investigated for two cells with aspect ratios $\Gamma=6.15$ and 5.01. We refer to them as cells 5 and 6, respectively (for details see Sec. III below). We found a primary bifurcation to a state with a *hexagonal* flow pattern. Within our resolution this bifurcation was nonhysteretic and the Nusselt number $\mathcal{N}$ grew continuously from zero. The appearance of hexagons rather than rolls is attributable to non-Boussinesq effects [18,19], which occur when the up-down symmetry is lifted by variations of the fluid properties over the cell height. Theoretically the bifurcation to hexagons is transcritical, and there should also be hysteresis associated with it. However, the hysteresis is often so small that it is unobservable even though hexagons are found over a substantial range [21]. At sufficiently large $\Delta T/\Delta T_c$ the hexagons become unstable with respect to rolls [19]. Since ΔT_c decreases with the cell thickness d ($\sim d^{-3}$), the range of stability of hexagons should depend on the thickness of the fluid sample. However, for the *thinner* fluid layer of cell 5, the existence range of hexagons was limited by a different secondary instability and grew from zero very near the TCP to $\epsilon\equiv\Delta T/\Delta T_c-1\simeq 0.1$ at the highest fields available to us. At this stability limit a hysteretic transition yielded the chaotic state, and stationary rolls were never found. With decreasing ΔT, the chaotic state persisted down to ΔT_s some-

what smaller than ΔT_c. For the thicker fluid layer of cell 6, typically ΔT_c was about 2 °C, and hexagons were found only up to $\epsilon \simeq 0.015$ even at high fields. For $\epsilon > 0.015$, a pattern of rolls *not* exhibiting STC was observed, as expected for a weakly non-Boussinesq system. At even higher ϵ and consistent with the measurements in cell 5, a hysteretic secondary bifurcation again yielded the chaotic state.

II. PARAMETER DEFINITIONS AND VALUES

The quantitative aspects of the instabilities are determined by four dimensionless parameters that are formed from combinations of the fluid properties [22]. They are [10] the Prandtl number

$$\sigma = \frac{(\alpha_4/2)}{\rho \kappa_\parallel}, \tag{1}$$

the ratio between the director-relaxation time and the heat-diffusion time

$$F = \frac{(\alpha_4/2)\kappa_\parallel}{k_{33}}, \tag{2}$$

the Rayleigh number

$$R = \frac{\alpha g \rho d^3 \Delta T}{(\alpha_4/2)\kappa_\parallel}, \tag{3}$$

and the dimensionless magnetic field

$$h = H/H_F \tag{4}$$

with the Fréedericksz field

$$H_F = \frac{\pi}{d}\sqrt{\frac{k_{33}}{\rho \chi_a}}. \tag{5}$$

In these equations α_4 is one of the viscosity coefficients, $\kappa_\parallel$ is the thermal diffusivity parallel to $\hat{n}$, k_{33} is one of the elastic constants of the director field, χ_a is the anisotropy of the diamagnetic susceptibility, α is the isobaric thermal expension coefficient, and g is the gravitational acceleration. The time scale of transients and pattern dynamics is measured in terms of the thermal diffusion time

$$t_v = d^2/\kappa_\parallel. \tag{6}$$

Both h and R are easily varied in an experiment, and may be regarded as two independent control parameters. The availability of h in addition to R makes it possible to explore an entire line of instabilities. The parameters F, σ, and t_v are essentially fixed once a particular NLC and temperature range have been chosen, and even between different NLCs there is not a great range at our disposal. For 5CB at 25.6° (the material and mean temperature used in this work), we have $\sigma = 263$ and $F = 461$. The value of t_v is typically several minutes, but depends on the thickness of the fluid layer. It is given in the next section for each of our cells. The critical value $R_c(h)$ of R and the fluid parameters determine the critical temperature difference ΔT_c for a sample of a given thickness d. The realistic experimental requirement that $\Delta T_c \simeq$ a few °C dictates that the sample thickness should be a few mm. Typical values of H_F are 10 to 20 G. Thus modest fields of a kGauss or so are adequate to explore the entire range of interest.

In order to evaluate R_c from ΔT_c, $h = H/H_F$, and the theoretical values for $R_c(h), k_c(h)$, and $\omega_c(h)$, we used the material properties given in Ref. [22]. We followed closely the calculational methods of FDPK. In order to ensure a sufficient resolution of any boundary layers we used Chebycheff modes in the Galerkin method (no more than 20 were required).

III. EXPERIMENTAL APPARATUS AND SAMPLE PREPARATION

The apparatus used in this work was described previously [23,14]. We made measurements using three circular cells of different thicknesses, identified as cells 4, 5, and 6 [24]. The thickness and radius were $d = 3.94$ mm, $r = 41.9$ mm for cell 4, $d = 6.60$ mm, $r = 40.6$ mm for cell 5, and $d = 8.88$ mm, $r = 44.5$ mm for cell 6. The corresponding radial aspect ratios $\Gamma \equiv r/d$ were 10.6, 6.15, and 5.01. The fluid was (5CB). All experiments were performed at a mean temperature of 25.6°C. The vertical thermal diffusion time was $t_v = 139$, 383, and 694 s, and H_F was 20.1, 12.6, and 9.34 G for cells 4, 5, and 6, respectively. Despite the longer time scales involved for experiments in the thicker cells, cells 5 and 6 had an advantage over cell 4 due to the smaller field strengths and temperature differences required to perform the measurements. To ensure homeotropic alignment near the surfaces of the top and bottom plates of both cells, a surface treatment with lecithin [6,14] was applied.

Defect-free homeotropic samples were prepared by applying a magnetic field while cooling the bath, and thus the sapphire top plate of the sample, from above the isotropic-nematic transition temperature T_{NI} to $T < T_{NI}$. During this process, the bottom plate naturally lagged behind, and thus an adverse density gradient existed. In the nematic-isotropic two-phase region even the relatively small thermal gradients associated with small cooling rates induced convection [25]. When the cooling was too rapid and the field too small this led to a nematic sample with defects which remained frozen. By using cooling rates of 1 °C/hour in the presence of a field of $h \geqslant 17$ over the temperature interval 36 to 34 °C ($T_{NI} = 35.1$ °C) and annealing at 34 °C for an hour or two the defects healed and a defect-free homeotropic sample could be prepared. Further cooling could then be at least ten times as rapid without introducing new defects because the threshold for convection in the nematic phase is large. Before each experimental run, the procedure was repeated.

The critical temperature differences for the onset of convection were determined from heat-transport measurements. These are usually expressed in terms of the Nusselt number

$$\mathcal{N} \equiv \lambda_{\rm eff}/\lambda_\parallel, \tag{7}$$

where $\lambda_\parallel$ is the conductivity of the homeotropically aligned sample [23], and

$$\lambda_{\rm eff} \equiv -Qd/\Delta T \tag{8}$$

is the effective conductivity and contains contributions from diffusive heat conduction and from hydrodynamic-flow ad-

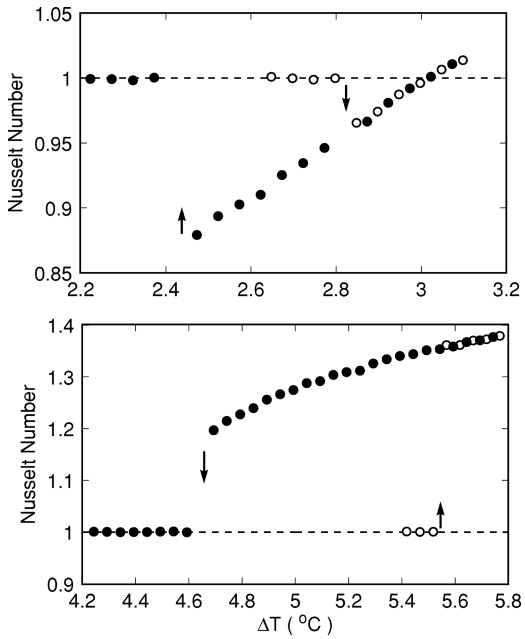

FIG. 1. Examples of the Nusselt number as a function of ΔT for cell 5. The upper figure is for $h=15$ and the lower one is for $h=50$. Open circles were taken with increasing and solid circles with decreasing ΔT. The transitions between conduction and convection are indicated by the arrows.

vection. Measurements of $\mathcal{N}$ were made by determining the heat current Q required to hold ΔT constant. At each ΔT, the heat current and temperature of the bath and bottom plate were measured at 1 min intervals for three to five hours, when typically all transients had died out.

In addition to heat-flow measurements, we also visualized the convective flow patterns. The homeotropic samples were translucent even for d as large as several mm. It was just about possible to see features of the bottom plate in typical ambient lighting. Any director distortion by convection rolls or domain walls generated opaque regions with enhanced diffuse scattering, which were easily visible. It should be kept in mind that the optical signal in the images has a complicated relationship to the hydrodynamic flow fields, and that quantitative information about velocity- or temperature-field amplitudes could not be obtained. Such quantities as the wave vector of the patterns or frequencies of traveling convection-rolls could of course be determined quantitatively.

The samples were illuminated from above by a circular fluorescent light. Digital images were taken from above by a video camera, which was interfaced to a computer. Typically 50 to 200 images were averaged to improve the signal-to-noise ratio. Averaged images were divided by an appropriate reference image to reduce the influence of lateral variations in illumination and of other optical imperfections. Some images were processed further by filtering in Fourier space.

IV. RESULTS

A. Nusselt numbers and critical Rayleigh numbers

Figure 1 shows $\mathcal{N}$ for cell 5 as a function of ΔT for two field strengths $h=15$ and $h=50$. The open circles were obtained with increasing, and the solid circles with decreasing

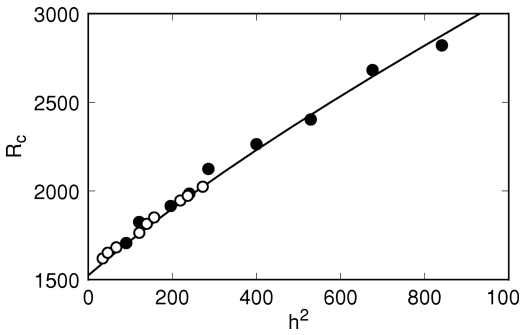

FIG. 2. Critical Rayleigh numbers for the onset of convection as a function of h^2. Open and filled symbols were obtained in cells 4 and 5, respectively. The line is the theoretical prediction.

ΔT. For the lower fields ($h<20$) $\mathcal{N}$ decreased below one when convection started. This can be understood because the convecting sample has a distorted director with a component perpendicular to $\vec{Q}$. The contribution from this component to the conductivity corresponds to $\lambda_\perp$, which is less than the conductivity $\lambda_\parallel$ of the homeotropic case [23]. It turns out that for small fields the direct hydrodynamic contribution to the heat flux is smaller than the decrease in the heat flux due to the director distortion by the flow. For the higher fields ($h>35$), $\mathcal{N}$ remained above one in the convecting state. Thus with the higher fields the hydrodynamic contribution to the heat flux is greater than the decrease in the heat flux due to any distortion of the director. Both examples in Fig. 1 demonstrate the predicted and previously observed [9,14,20] hysteretic nature of the bifurcation, i.e., as ΔT was decreased, the conduction state was reached at a value of ΔT equal to $\Delta T_s<\Delta T_c$.

From data like those in Fig. 1, critical temperature differences ΔT_c were determined with an uncertainty of less than 1%. The corresponding Rayleigh numbers are shown in Fig. 2 as a function of h^2. The open circles were obtained in cell 4, the filled ones in cell 5. The good agreement between the two data sets confirms the expected scaling of the field with H_F. It also shows that using the fluid properties at the mean temperature does not lead to systematic errors in R_c even for cell 4 where ΔT_c is over 10 °C. One sees that R_c is quadratic in h at small h, as is expected because the system should be invariant under a change of the field direction. The solid line follows the theoretical prediction and agreement between theory and experiment is excellent.

Results for R_c over our full experimental field range are shown as a function of h in Fig. 3. Here we include data taken with cell 6 as open squares. The data for R_c reveal a sharp maximum at $h=44.3$. We interpret this field value as the codimension-two point h_{ct} and indicate it in Fig. 3 by the dashed vertical line. The solid line in the figure is the theoretical prediction for R_c, evaluated for the properties of our sample. For the entire range $h<h_{ct}$, the theoretical result is in excellent agreement with the data. However, the theory gives $h_{ct}=41.8$, which is slightly lower than the experimental value. Above h_{ct} the measurements of R_c are systematically larger than the calculation, although the largest discrepancy is only about 4%.

The triangles in Fig. 3 show the lower limit of existence (the ''saddle-node'' Rayleigh number R_s) of the finite-

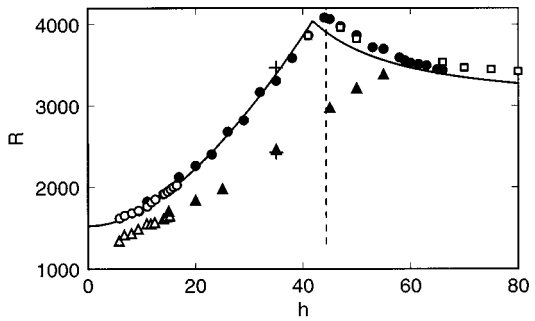

FIG. 3. Critical Rayleigh numbers R_c and saddle-node Rayleigh numbers R_s over the experimentally accessible field range. The open circles, filled circles, and open squares are R_c for cells 4, 5, and 6, respectively. The open and filled triangles are R_s for cells 4 and 5, respectively. The dashed line indicates the location of the codimension-two point as found experimentally. The solid line is the theoretical prediction for R_c. The plusses at $h=35$ were obtained with short equilibration times and cell 5 (see text).

amplitude convecting state as determined from data like those in Fig. 1. They suggest that the tricritical bifurcation is located near $h=59$, which is larger than the theoretically calculated value $h_t \simeq 51$. However, we will return later to the best estimate of h_t.

Measurements similar to those shown in Fig. 3 were made by Salán and Fernández-Vela [20] (SF), using the nematic liquid crystal MBBA. Their results are shown in Fig. 4, together with the theoretical curve for that case [26]. The data and the curve illustrate that there are significant quantitative differences between the bifurcation lines of different nematics. In Fig. 4 the experimental points lie on average about 25% above the theoretical curve, and the lower hysteresis limit is further below the bifurcation line than we found for 5CB.

The equilibration times after each temperature step used by SF were 30 min, which is a factor of six to ten shorter than those of our experiments. In addition the temperature steps of SF were a factor of two larger than ours, yielding a difference in the average rate of change of the temperature of a factor of 12 or more. Looking for an explanation of the difference between the experimental and theoretical R_c revealed in Fig. 4, we conducted one run with equilibration times similar to those of SF, but using our 5CB sample. It gave the plusses in Fig. 3. As can be seen, these results do not differ significantly from the data taken with our usual

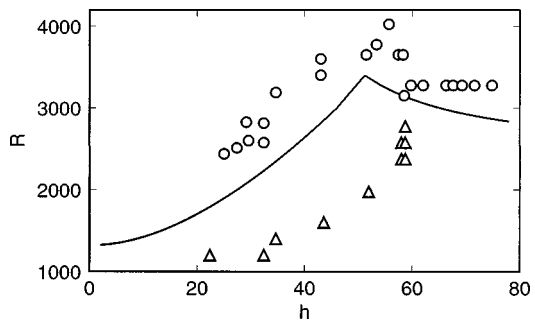

FIG. 4. Results for R_c and R_s from Ref. [20] obtained with MBBA. The theoretical curve for R_c was computed from typical fluid properties of MBBA [26].

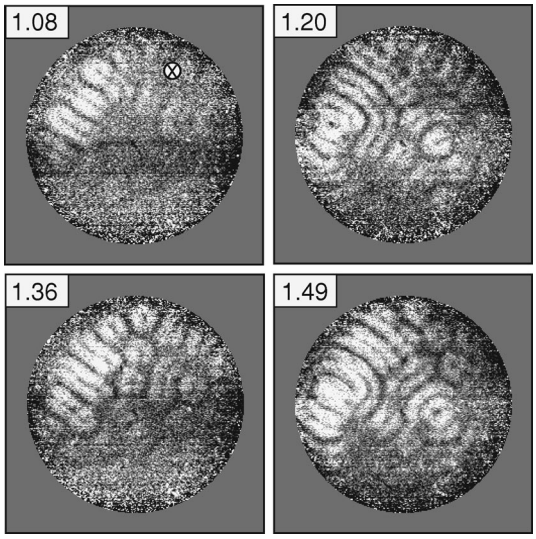

FIG. 5. A sequence of images of the travelling or standing wave transients for $h=32$ and $\epsilon=0.015$ in cell 5. The number in each image corresponds to the time, in units of t_v, that elapsed since flow first became visible. A time series of the pixel intensity was taken at the location marked in the top left image.

longer equilibration times. Thus we have no explanation for the difference between the SF data for R_c and the theoretical curve. However, the agreement between our runs with the different equilibration times implies that our usual experimental procedure yielded quasi-static results.

B. Hopf frequency and critical wave vector

Once the critical Rayleigh numbers were measured, a detailed analysis of the patterns could be undertaken. At first we will characterize the Hopf bifurcation for h below h_{ct}. Since in that field range the bifurcation is subcritical, we had to use the small-amplitude transients to determine ω_c and k_c. Figure 5 shows images from cell 5 that are characteristic of these patterns. They were taken at the times (in units of $t_v=383$ s) indicated in each figure after the pattern initially became visible. This typically occurred around 1 h after ϵ was raised from below zero to around 0.015. Inspection of successive images revealed that the transients could be either traveling or standing waves, sometimes with both occurring at different locations in the same cell. In the top left image of Fig. 5, a location is indicated at which a time series of the pixel intensity was acquired. This time series is shown in Fig. 6 along with its corresponding power spectrum. The length of the time series was limited by the rapid growth of the pattern to its finite-amplitude steady state. Because of this, only a small number of periods could be obtained before the finite-amplitude state was reached. Thus to avoid errors associated with incommensurate sampling, the data were windowed before its Fourier transform was evaluated. This process was repeated at several pixel locations in the cell. The signal from the second harmonic was often found to be stronger than that from the fundamental. Thus it was used to calculate the frequency. The frequencies at different locations generally were within 1% of each other, and were averaged to determine the critical Hopf frequency ω_c.

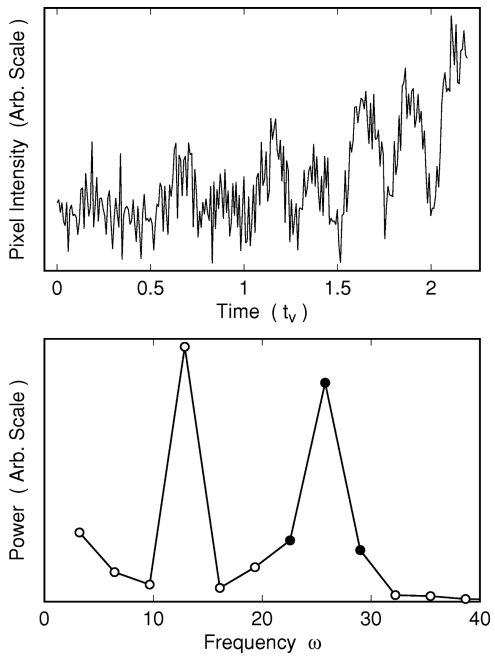

FIG. 6. The upper figure is the time series of the pixel intensity at the location shown in the top left image of Fig. 5. The lower figure is the power spectrum of that time series. The mean frequency calculated from the solid circles was used to determine the Hopf frequency.

The dependence upon h of the measured ω_c is compared with theory in Fig. 7. The arrow indicates the location of the theoretical codimension-two point while the dashed line represents the experimental determination of h_{ct}. As can be seen, away from the codimension-two point the agreement with the measurements is excellent. In accordance with theory, the experimental ω_c changes discontinuously to zero at h_{ct}, above which the bifurcation is stationary.

By evaluating the Fourier transforms of images such as those in Fig. 5, the critical wave number k_c of the patterns could be measured. The transforms were based on the central parts of the images by using the filter function $W(r)=\{1+\cos[(\pi)(r/r_0)]\}/2$ for $r<r_0$ and $W(r)=0$ for $r>r_0$. Here r_o was set equal to 85% of the sample radius. Time averaging the square of the modulus of the transforms over the length of the time series yielded the structure factor $\langle S(\mathbf{k})\rangle$.

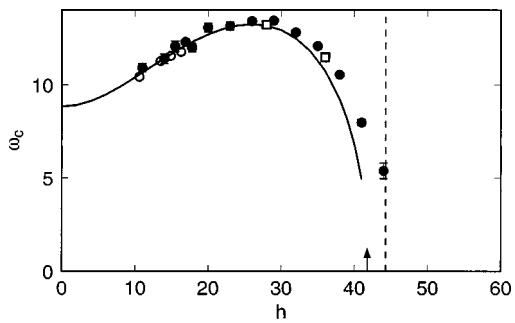

FIG. 7. The Hopf frequency ω_c as a function of h. Open and filled circles are for cells 4 and 5, respectively. Open squares are for cell 6. The solid line is the theoretical prediction for ω_c. The dashed line (arrow) indicates the location of the codimension-two point as found experimentally (theoretically).

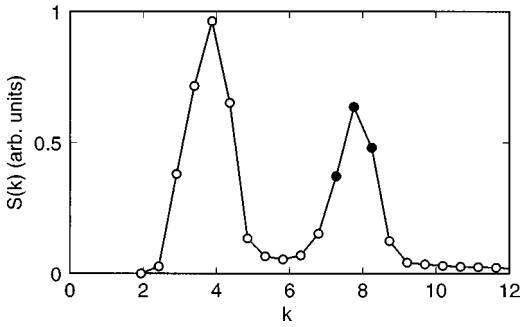

FIG. 8. The azimuthal average of the time-averaged structure factor $\langle S(k)\rangle$ of the travelling/standing wave transients at $h=32$ for cell 5. The mean wavenumber calculated from the solid circles was used as the critical wave number.

Figure 8 shows the azimuthal average $\langle S(k)\rangle$ of $\langle S(\mathbf{k})\rangle$ for the run at $h=32$. We used a weighted average of the three points nearest the peak of the second harmonic of $\langle S(k)\rangle$ to calculate k_c.

Figure 9 displays the results for k_c for all h together with the theoretical analysis. For $h<h_{ct}$ the measured critical wave number of the transients is systematically smaller than the theoretical one. When the codimension-two point is approached, the experimental wave numbers make a smooth rather than discontinuous transition to those associated with the stationary bifurcation, whereas the theory predicts a 7% discontinuity of k_c at h_{ct}. The reason for these discrepancies is as yet unknown. Above h_{ct}, the agreement between the experimental and theoretical wave numbers is excellent.

As shown explicitly for R_c in Fig. 2, R_c, ω_c, and k_c are proportional to h^2 for small h.

C. Nonlinear state below the tricritical field h_{ct}

Because of the subcritical nature of the bifurcation for $h<h_{ct}$ a finite-amplitude state develops directly at onset. The time dependence and spatial structure of this state are very different from that of the small-amplitude transient state. The first two rows of Fig. 10 show typical images of the patterns from cell 5 that are characteristic of the fully developed flow. They are from a single experimental run with constant external conditions. They were taken at the times indicated in

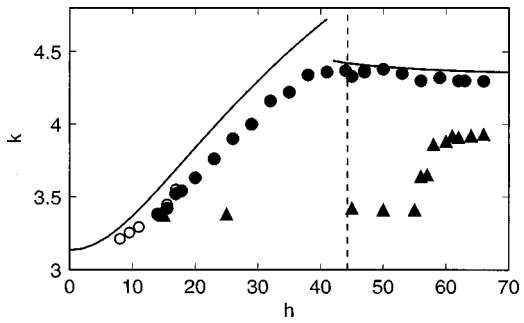

FIG. 9. The characteristic wave numbers of the observed patterns as a function of h. Circles: The wave number of the small-amplitude transients. Triangles: The wave number k_n of the fully developed spatially and temporally chaotic flow, as measured close to the onset of such flows. Open and filled symbols were obtained in cells 4 and 5, respectively.

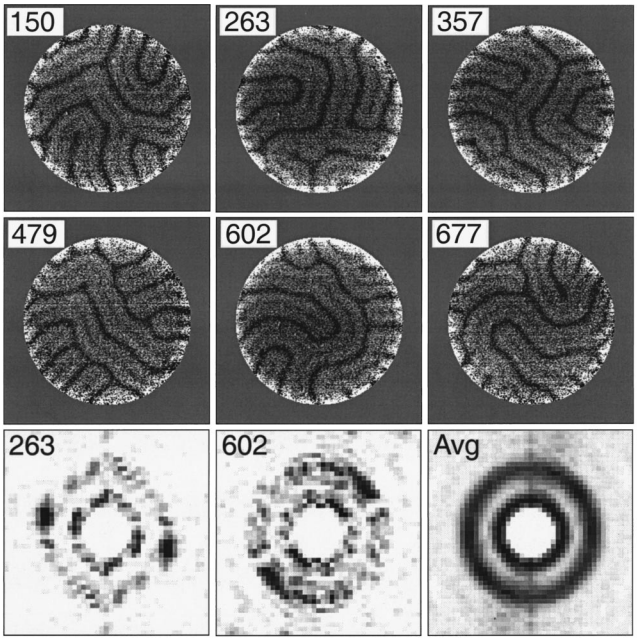

FIG. 10. Top two rows: a sequence of images taken with constant external conditions ($h=50$, $\epsilon=0.014$) for cell 5. The time elapsed since ϵ was raised from below zero (in units of $t_v=383s$) is given in the top left corner of each image. Bottom row: The structure factor of two of the images shown above, and the average of the structure factor of 75 images spanning a time interval of $724t_v$. The structure factor was obtained using a Hanning window, and thus is dominated by the patterns near the cell center.

each image, in units of $t_v=383$ s, which had elapsed since ϵ had been raised from below zero to 0.014. The convection rolls of the fully developed flow show an irregular time dependence, with typical time scales around 100 times longer than the inverse Hopf frequencies of the transients. One can see that the ''chaotic'' behavior is associated with the formation of defects and the continuous reorientation of the convection rolls. This continuous reorientation of the rolls is evident in the rightmost image in the bottom row of Fig. 10 (labeled ''Avg''). It shows the time average of the structure factor. The average involved 75 images taken over a total time period of $724t_v$ (over three days). It is seen to contain contributions at all angles, consistent with the idea of a statistically stationary process of nonperiodic pattern evolution and with the expected rotational symmetry of the system. Similar results for cell 4 have been shown previously [14].

When h was increased above $h_{\rm ct}$, the nature of the pattern at first did not change noticeably. For instance, as evident in Fig. 9, the characteristic wave number of the pattern (as denoted by the triangles) remained close to 3.4 for $h\leqslant 55$. Over this field range the patterns of the fully developed flow look similar to those illustrated in Fig. 10, i.e., they exhibit spatiotemporal chaos.

It is instructive to examine the transients that lead from the small amplitude to the finite-amplitude statistically stationary state. This is done in Fig. 11. Here the number in each image gives the time, in units of t_v, which had elapsed since ΔT was raised slightly (1.4%) above ΔT_c. At $t=4.7$ small-amplitude transients like those in Fig. 5 are evident in part of the cell. By $t=9.4$ these had filled the cell and grown to a saturated amplitude. At this stage they formed nearly

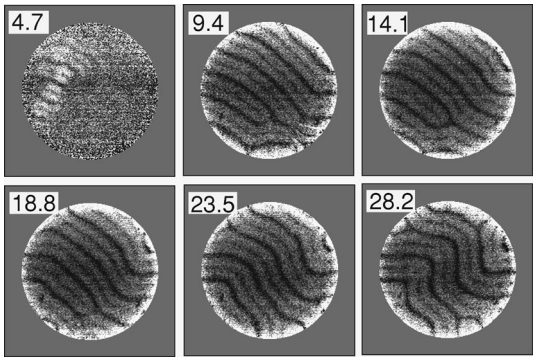

FIG. 11. A temporal succession of images during the transient leading from conduction to convection when ΔT was raised slightly above ΔT_c for cell 5. The field was $h=50$. The numbers are the elapsed time, in units of t_v, since the threshold was exceeded.

straight parallel rolls with a wave number that was smaller than k_c. However, these straight rolls turned out to be unstable to a zig-zag instability. In the end, this instability led to the spatially and temporally disordered pattern as shown in Fig. 10. Thus, we see that a secondary instability led to a chaotic state rather than to a new time-independent pattern. This phenomenon most likely is similar to the one encountered in very early experiments on spatiotemporal chaos using liquid helium [27,28], where ordinary RB convection became chaotically time dependent, most likely because the secondary skewed-varicose instability [29] was crossed.

Heat-transport measurements of the fully developed flow are shown in Fig. 12 for several field values as a function of ϵ. They illustrate the evolution with h of the hysteretic nature of the bifurcation. As can be seen also in Fig. 3, the hysteresis $|\epsilon_s|$ increased with h for $h<h_{\rm ct}$ from about 10% at the low fields to nearly 25% close to the codimension-two point. Above this point the hysteresis decreased and suggested the existence of a tricritical point near $h_t\simeq 59$ (see below for more detail about the tricritical region).

When the Nusselt numbers in Fig. 12 are plotted against the Rayleigh number R, they fall on or approach a single curve independent of h. This suggests that the convection in the chaotic state is sufficiently vigorous to achieve nearly complete randomization of the director orientations, regardless of h. In that case one would expect that the system should behave approximately like an isotropic fluid, with an averaged conductivity $\lambda_{\rm avg}=(2\lambda_\perp+\lambda_\parallel)/3$. Thus we plot in Fig. 13 a modified Nusselt number $\tilde{\mathcal{N}}$ given by the ratio of the effective conductivity of the convecting state to $\lambda_{\rm avg}$ as a function of $R_{\rm avg}$, where $R_{\rm avg}$ is computed using $\kappa_{\rm avg}=\lambda_{\rm avg}/\rho C_P$ in Eq. (3) rather than $\kappa_\parallel$. At all but the highest fields (where the primary bifurcation is supercritical) the data reach the common curve. At small $R_{\rm avg}$, this curve extrapolates to $\tilde{\mathcal{N}}=1$ near $R_{\rm avg}=1708$ (the cross in the figure), which is the critical Rayleigh number of an isotropic fluid. An analogous behavior has been observed in binary-mixture convection with negative separation ratios Ψ [30], where the bifurcation is also subcritical. In that case the convective flow achieves thorough mixing of the concentration field and $\mathcal{N}$ approaches a curve that is independent of Ψ. In both cases the mixing achieved by the flow can persist because of the existence of a slow time scale, namely, that of

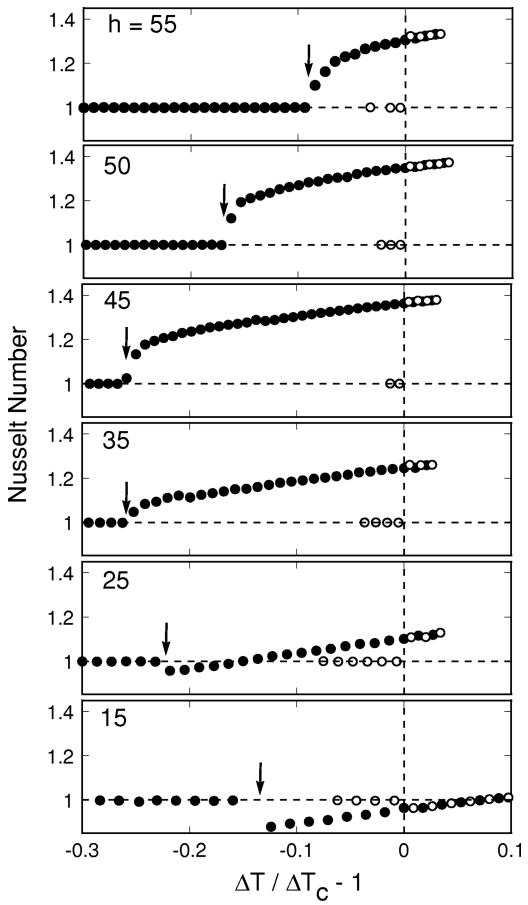

FIG. 12. Nusselt-number measurements for cell 5 illustrating the variation of the size of the hysteresis loop between conduction and convection with h. The number in the upper left corner of each plot is the field h. Open circles were taken with increasing and solid circles with decreasing ΔT. The arrows show the values of $\epsilon_s \equiv R_s/R_c - 1$.

director or concentration relaxation.

Further support for the idea that the chaotic flow in some respects can be approximated by isotropic-fluid convection is found in Fig. 9, where for $h \lesssim 55$ the wave vectors (triangles) are independent of h and much closer to the critical value $k_c^{\rm iso} = 3.117$ than to the critical values $k_c(h)$ of the anisotropic system (circles in Fig. 9). Exact agreement with $k_c^{\rm iso}$ would of course not be expected even for a genuine isotropic fluid because of the finite flow amplitude and various wave number-selection processes.

Lastly we note that an extrapolation of the data in Fig. 13 to $\tilde{\mathcal{N}} = 1$ and $R_{\rm avg} = 1708$ yields an initial slope $\tilde{S}_1$ of $\tilde{\mathcal{N}} - 1 = \tilde{S}_1(R_{\rm avg}/1708 - 1)$ of about 0.6. For a laterally infinite system of straight rolls in an isotropic fluid with a large Prandtl number one expects $S_1 \simeq 1.43$ [31]. However, experiments in finite systems with modest aspect ratios [32] have always yielded smaller values, usually in the range of 0.6 to 1. Particularly when many defects are present, as in our case, one would expect the heat transport to be suppressed relative to that of a perfect straight-roll structure.

D. Tricritical region and beyond

This section is devoted to the phenomena that occur near the tricritical field $h = h_t$. At first the Nusselt numbers and the patterns are described and the corresponding bifurcation diagram is given. Further subsections deal with the precise determination of h_t and with hexagons observed near threshold for $h > h_t$.

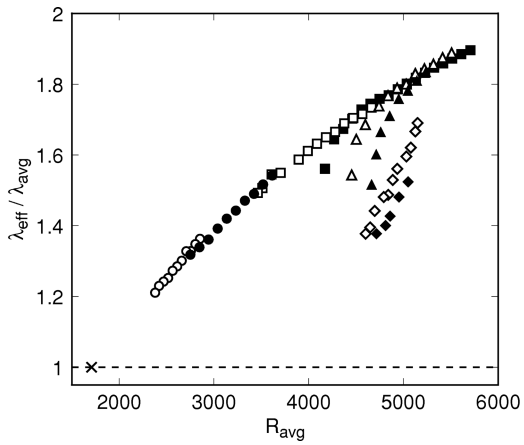

FIG. 13. Nusselt-number measurements for cell 5, normalized by the averaged conductivity $\lambda_{\rm avg} \equiv (2\lambda_\perp + \lambda_\parallel)/3$, as a function of the Rayleigh number $R_{\rm avg}$ computed with $\kappa_{\rm avg} \equiv \lambda_{\rm avg}/\rho C_P$. The data are for $h = 15$ (open circles), 25 (solid circles), 35 (open squares), 45 (solid squares), 50 (open triangles), and 55 (solid triangles). The diamonds are for $h = 64$, which is in the supercritical region. Here the solid diamonds are for the hexagons or rolls, which form supercritically, and the open ones are for the chaotic finite-amplitude state, which forms via a secondary bifurcation (see Fig. 19 below). The cross corresponds to the critical Rayleigh number $R_c = 1708$ of an isotropic fluid.

1. Nusselt numbers and patterns

From the measurements of the Nusselt number (see Fig. 12) there is clear evidence of a tricritical field h_t, above which the primary bifurcation is supercritical. For instance, for $h \simeq 60$, measurements of $\mathcal{N}$ revealed no hysteresis at the primary bifurcation and within our resolution $\mathcal{N}$ grew continuously from one beyond ΔT_c. This is exemplified for cell 5 and $h = 63$ in Fig. 14. The open (solid) circles correspond to the stable states reached by increasing (decreasing) ΔT [33]. This behavior of $\mathcal{N}$ stands in sharp contrast to that shown in Fig. 12 for lower fields.

Besides the Nusselt number the analysis of the patterns gives important additional insight in particular with respect

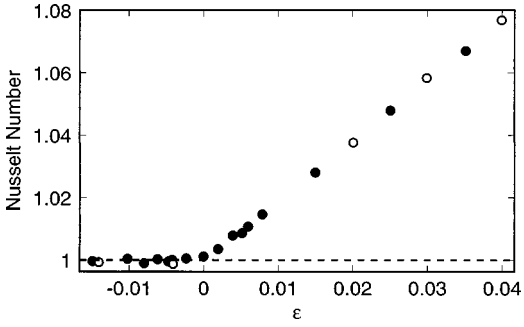

FIG. 14. Nusselt-number measurements for $h = 63$ and cell 5 illustrating the supercritical nature of the bifurcation characteristic of the high fields. Open circles were taken with increasing and solid circles with decreasing ΔT.

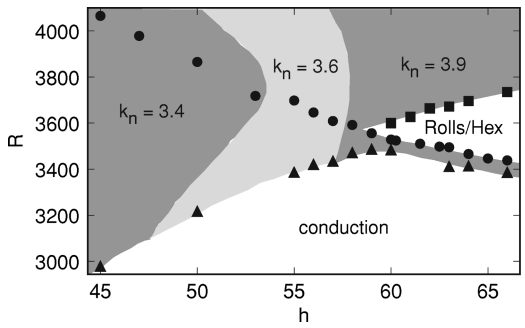

FIG. 15. Bifurcation diagram in the region of the R-h plane close to the tricritical point. Solid circles: primary bifurcation. Solid triangles: R_s. Solid squares: hysteretic secondary bifurcation to chaotic convection. Shaded areas labeled $k_n=3.4$, 3.6, and 3.9 correspond to chaotic regimes with different mean wave numbers. The wedge-shaped area labeled Rolls/Hex shows the parameter range over which time-independent convection is stable. For cell 5, the pattern is hexagonal in this entire region. For cell 6, the pattern is hexagonal in this region for $\epsilon \leqslant 0.015$. For larger ϵ but still in this region it consists of time-independent rolls.

to secondary transitions. In Fig. 15 all the available information has been condensed in a bifurcation diagram for the vicinity of the tricritical point.

At first we will focus on the wedge labeled Rolls/Hex where time-independent convection is stable. For both cell 5 and 6, a seemingly supercritical primary bifurcation led to a hexagonal pattern. For cell 5 this pattern is shown in Fig. 16. The range of ϵ over which the hexagons were stable differed in the two cells. In cell 5, hexagons remained stable up to $R_n(h)$ (solid squares in Fig. 15) for the entire range of h. At $R_n(h)$ a transition to a spatially and temporally chaotic roll pattern with a lower characteristic wave number occurred. For $h<75$ this transition was distinguished by a jump in $\mathcal{N}$ as well as the onset of time dependence of $\mathcal{N}$, as illustrated in Fig. 17. The upper figure gives the steady-state $\mathcal{N}$ and shows the jump at $\epsilon_n \equiv R_n/R_c - 1$. The lower figure is the time series of $\mathcal{N}$ obtained in the same run. Here ϵ was held

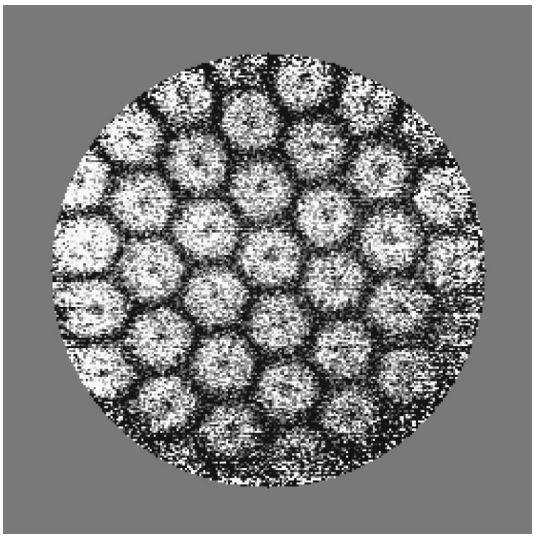

FIG. 16. Image of the hexagonal flow in cell 5 for $h=65$ and $\epsilon=0.01$. The pattern was essentially the same over the entire existence range of hexagons.

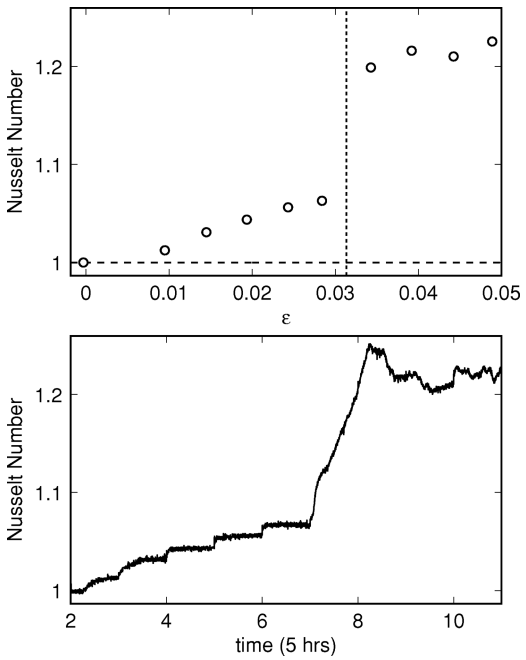

FIG. 17. Nusselt-number measurements for $h=61$ in cell 5. The upper figure illustrates the dependence of the Nusselt number on ϵ. The dotted line indicates ϵ_n, where the transition from hexagons to rolls occurred when ΔT was increased. The lower figure illustrates the dependence of the Nusselt number on time. Time is measured in units of 5 h, i.e., the time between steps in ϵ.

constant for a 5 h period at each of the eleven successively increasing values. The data show that $\mathcal{N}$ is steady below and time dependent above $\epsilon_n(h)$. For $h \geqslant 75$ the discontinuity in $\mathcal{N}$ was no longer pronounced, but a transition to time dependence still occurred at $\epsilon_n(h)$. Thus, depending on the field, either of these two indicators was used to determine the location of $\epsilon_n(h)$. In the thicker cell 6, a transition from hexagons to rolls occurred near $\epsilon \simeq 0.015$, independent of field strength. This transition was not associated with a measurable change in the wave number, a jump in $\mathcal{N}$, or a time dependence of $\mathcal{N}$. A further increase of ϵ again led to a transition at $\epsilon_n(h)$ from steady rolls to the chaotic state, consistent with the cell 6 experiments. The results for $\epsilon_n(h)$ obtained in cells 5 and 6 are shown in Fig. 18 as circles and triangles respectively.

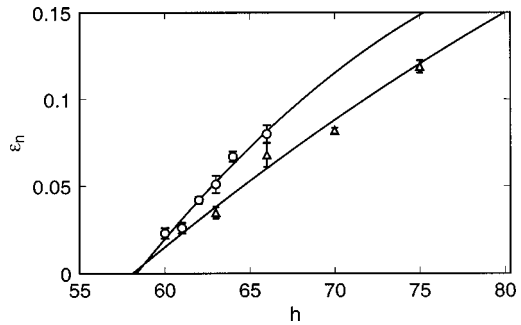

FIG. 18. Values of $\epsilon_n(h)$ where a transition to a spatially and temporally chaotic state occurred. Circles and triangles were obtained in cells 5 and 6, respectively. The lines represent a fit of a quadratic polynomial in $(h/h_n - 1)$ to the data. The fits extrapolate to zero at $h_n = 58.3 \pm 0.7$ for cell 5 and $h_n = 58 \pm 3$ for cell 6.

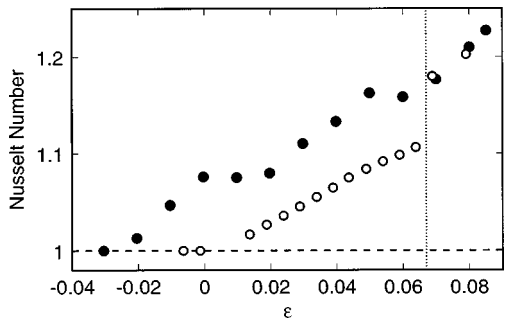

FIG. 19. Nusselt-number measurements for $h=64$ in cell 5. Open circles were taken with increasing and solid circles with decreasing ΔT. The dotted line indicates ϵ_n.

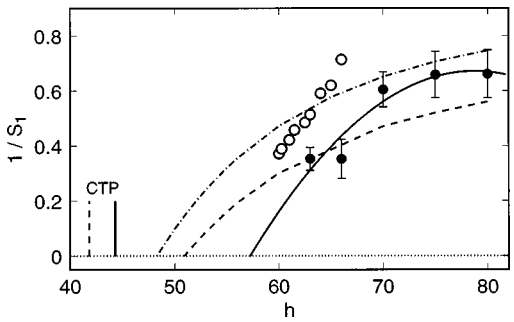

FIG. 20. The dependence on h of the reciprocal of the initial slope S_1 of the Nusselt number as obtained from a fit of the data to Eq. (9). The open circles are $1/S_{1,h}$ for cell 5, and the filled ones are $1/S_{1,r}$ for cell 6. For cell 5, data over the range $0<\epsilon<\epsilon_n$ were used, and the pattern was hexagonal. For cell 6, data over the range $0.015<\epsilon<\epsilon_n$ were used, and the pattern was one of rolls. The solid line represents a fit of a quadratic polynomial in (h/h_t-1) to the cell 6 $S_{1,r}$ data. The field $h_t=57.2\pm2.6$, where $1/S_{1,r}$ for cell 6 extrapolates to zero, is interpreted to be the tricritical point. The theoretical results for $1/S_{1,r}$ are given by the dashed line. They yield a tricritical point at $h_t^{th}=51$. The theoretical results for $1/S_{1,h}$ are given by the dash-dotted line. The location of the codimension-two point is given by the solid (experimental) and dashed (theoretical) short vertical lines.

On the basis of the usual Landau equation for a tricritical bifurcation, one would expect the hysteresis to grow gradually as h is reduced below h_t. However, within our resolution this was not the case and a hysteretic primary bifurcation to a chaotic state occurred immediately below h_t. Indeed, the secondary bifurcation line $\epsilon_n(h)$ for $h>h_t$ met the primary bifurcation line at h_t within experimental resolution, as can be seen already in Fig. 15.

It is shown more explicitly in Fig. 18, where the range ϵ_n of time-independent patterns vanishes near $h=58$. Fitting a quadratic polynomial in (h/h_n-1) to $\epsilon_n(h)$ yields $h_n=58.3\pm0.7$ (cell 5) and $h_n=58\pm3$ (cell 6) for the field where ϵ_n vanishes. Within error, these values agree with the tricritical field obtained from the slope of the Nusselt number (see the next section).The bifurcation for $h>h_t$ is supercritical but the amplitude at constant $\epsilon>0$ diverges as h approaches h_t from above. Since secondary bifurcations occur at finite values of the amplitude, we expect $\epsilon_n(h)$ to vanish at h_t. Therefore the ϵ_n measurements provide a relatively precise lower limit $h_t=57.6$ for the tricritical field.

The secondary bifurcation at ϵ_n is strongly hysteretic. As illustrated in Fig. 19, when ϵ was decreased from $\epsilon\geqslant\epsilon_n$, a transition back to hexagons did not occur. Instead, the chaotic state persisted to values of ϵ slightly below zero, at which point the conduction state was reached (see also the solid triangles in Fig. 15). In a separate section we will come back to the hexagons.

2. Determination of the tricritical point

As h approaches the tricritical point from above, the initial slope $S_{1,r}$ of $\mathcal{N}$ for rolls is expected to diverge as $1/(h-h_t)$. For cell 6, we estimated $S_{1,r}(h)$ from data for $\epsilon\gtrsim0.015$ where rolls were observed. At a given h, $S_{1,r}$ was determined by fitting the polynomial

$$\mathcal{N}=1+S_{1,r}\epsilon+S_{2,r}\epsilon^2 \tag{9}$$

with $\epsilon=\Delta T/\Delta T_c-1$ to the data. The parameters ΔT_c, $S_{1,r}$, and $S_{2,r}$ were adjusted in the fit. Figure 20 shows the dependence of $1/S_{1,r}$ upon h as solid circles. The fitting procedure did not yield highly accurate values because the Nusselt data for $\epsilon<0.015$ had to be excluded; thus the error bars for $S_{1,r}$ are relatively large. The line is a fit of a quadratic polynomial in (h/h_t-1) to the results for $1/S_{1,r}(h)$. This fit indicates the tricritical point to be at $h_t=57.2\pm2.6$.

In order to compare the theory with the measurements above h_t, we calculated $S_{1,r}$ using the properties of 5CB. The results for $1/S_{1,r}$ are shown as a dashed line in Fig. 20. There is quite reasonable agreement with the experimental data for $h\gtrsim60$, particularly when it is considered that the initial slope of $\mathcal{N}$ in finite systems usually is smaller than the theoretical value for the infinite system. However, the theory yields a tricritical field $h_t^{\rm th}=51$, which differs significantly from the experimental estimates. We note that this difference is in the same direction as and somewhat larger than the corresponding one for the codimension-two point. We have no explanation for this difference.

3. Hexagons

In this section we will discuss in more detail the hexagonal patterns. Hexagonal patterns at onset may be attributable to departures of the physical system from the Oberbeck-Boussinesq (OB) approximation [18,19], i.e., to a variations of the fluid properties over the imposed temperature range. For isotropic fluids it has been shown that non-OB effects lead to hexagons at a transcritical (hysteretic) primary bifurcation [19,21]. Below onset, for $\epsilon_a\leqslant\epsilon\leqslant0$, both hexagons and the conduction state are stable. Above onset, hexagons are stable for $0\leqslant\epsilon\leqslant\epsilon_r$. For $\epsilon_r\leqslant\epsilon\leqslant\epsilon_b$ hexagons and rolls are both stable, while for $\epsilon\geqslant\epsilon_b$ only rolls are stable. When the thickness of the fluid layer is increased, ΔT_c is reduced and thus departures from the OB approximation become smaller. Thus the range of ϵ over which hexagons are stable is reduced when the thickness of the fluid layer is increased, as seen in the experiment by comparing cells 5 and 6.

A stability analysis of RBC with non-OB effects in a homeotropically aligned NLC has not yet been carried out and would be very tedious. Thus, in order to obtain at least a qualitative idea of the expected range of stable hexagons, we used the theoretical results for the isotropic fluid with the

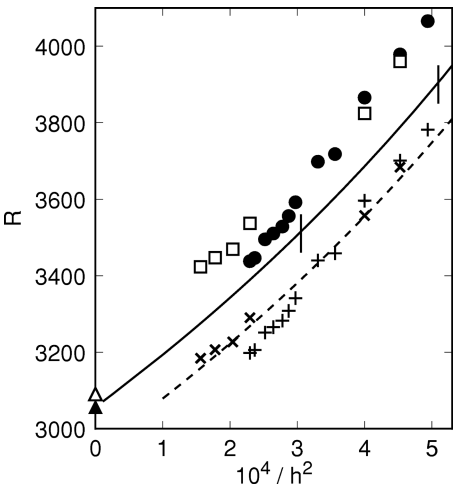

FIG. 21. The critical Rayleigh number as a function of $1/h^2$. The solid line was calculated using the parameters of Ref. [22]. The open triangle is $R_{c,\infty}$ from Eq. (13). The solid triangle is the many-mode numerical result for $R_{c,\infty}$. The solid circles are from cell 5, and the open squares are from cell 6. The vertical bars indicate the location of the codimension-two point (right bar) and the tricritical point (left bar). The plusses, crosses, and dashed line show what happens to the data and the theoretical curve if the viscosity α_4 is increased by 7.5%.

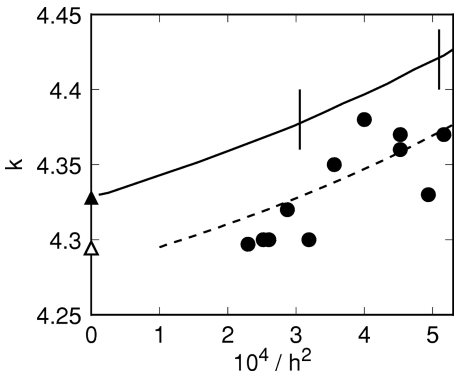

FIG. 22. The critical wave number as a function of $1/h^2$. The solid line was calculated using the parameters of Ref. [22]. The open triangle is $k_{c,\infty}$ from Eq. (13). The solid triangle is the many-mode numerical result for $k_{c,\infty}$. The vertical bars indicate the location of the codimension-two point (right bar) and the tricritical point (left bar). The dashed line shows what happens to the theoretical curve if the viscosity α_4 is increased by 7.5% (the data for k_c remain unchanged).

fluid properties of 5CB. The values of ϵ_a, etc. are determined by a parameter $\mathcal{P}$, which was defined by Busse [19] and is given by $\mathcal{P}=\Sigma_{i=0}^{4}\gamma_i\mathcal{P}_i$, with $\gamma_0=-\Delta\rho/\rho$, $\gamma_1=\Delta\alpha/2\alpha$, $\gamma_2=\Delta\nu/\nu$, $\gamma_3=\Delta\lambda/\lambda$, and $\gamma_4=\Delta C_P/C_P$. Here ρ is the density, α the thermal expansion coefficient, ν the kinematic viscosity, λ the conductivity, and C_P the heat capacity. The quantities $\Delta\rho$, etc. are the differences in the values of the properties at the bottom (hot) and top (cold) end of the cell. For λ we used $\lambda_\parallel$, and for ν we used $\alpha_4/2\rho$. The coefficients $\mathcal{P}_i$ in the equation for $\mathcal{P}$ are given by Busse [19]. However, here we use the more recent results [34] for large Prandtl numbers $\mathcal{P}_0=2.676$, $\mathcal{P}_1=-6.631$, $\mathcal{P}_2=2.765$, $\mathcal{P}_3=9.540$, and $\mathcal{P}_4=-6.225$ where $\mathcal{P}_3$ differs significantly from the earlier calculation.

At the fields where the hexagons were observed, the temperature difference across cell 5 (cell 6) was close to 5.05 °C (2.07 °C). At these temperature differences, we obtained $\mathcal{P}=-1.5$, $\epsilon_a=-1.7\times10^{-4}$, $\epsilon_r=1.5\times10^{-2}$, and $\epsilon_b=5.3\times10^{-2}$ for cell 5. For cell 6 the values are $\mathcal{P}=-0.6$, $\epsilon_a=-2.8\times10^{-5}$, $\epsilon_r=2.5\times10^{-3}$, and $\epsilon_b=8.7\times10^{-3}$. From these estimates, it follows that the hysteresis of size ϵ_a is too small to be noticeable in either cell with our resolution. The largest value of ϵ at which hexagons could exist in cell 6 would be $\epsilon=8.7\times10^{-3}$. However, we observe hexagons to exist to nearly twice this value. If the same is true for the thinner cell, the hexagon-roll transition attributable to non-OB effects should happen at a value of ϵ greater than $\epsilon_n(h)$ for the field range over which the experiments were performed. Thus, instead of leading to a time independent state, as observed in cell 6, the hexagon-roll transition is preceded by a transition to a state exhibiting spatio-temporal chaos at ϵ_n.

The hexagonal pattern may be regarded as a superposition of three sets of rolls with amplitudes A_i, $i=1,2,3$, corresponding to the three basis vectors at angles of 120° to each other. According to the Landau model [13] the steady-state amplitudes A_i are determined by

$$\epsilon A_1+\tfrac{1}{2}b(A_2^2+A_3^2)-g_{11}A_1^3-g_{12}A_1A_2^2-g_{13}A_1A_3^2=0 \tag{10}$$

and the corresponding cyclic permutation for $i=2,3$. Since all amplitudes are expected to be equal in hexagons ($A_1=A_2=A_3=A$), one has

$$\epsilon A+bA^2-(g+2\tilde{g})A^3=0, \tag{11}$$

where g is the self-coupling coefficient g_{11} and $\tilde{g}$ is the cross-coupling coefficient $g_{12}=g_{13}$. Because of the term bA^2, the bifurcation is transcritical and thus hysteretic. However, as we discussed above and as is shown, for instance, by the data in Fig. 14, this effect is not resolved in the experiment because the coefficient b (which is determined by $\mathcal{P}$) is too small. Thus we neglect the term bA^2, and have to a good approximation

$$\mathcal{N}-1=3A^2=\frac{3\epsilon}{g+2\tilde{g}}. \tag{12}$$

At the tricritical point g vanishes as $g=g_0(h-h_t)$. However, there is no reason why $\tilde{g}$ should vanish also at h_t. Thus, one would expect the slope $S_{1,h}=3/(g+2\tilde{g})$ of $\mathcal{N}$ near $\epsilon=0$ to remain finite at h_t and equal to $3/2\tilde{g}$. To test this idea, we fitted $\mathcal{N}$ for cell 5 over the ϵ range where hexagons were observed (i.e., up to ϵ_n) to an equation like Eq. (9). Since data quite close to threshold could be used, the results for $S_{1,h}$ are much more precise than those for cell 6. They are given in Fig. 20 as open circles. One can see that $1/S_{1,h}$ is non-zero at h_t. It extrapolates to zero near $h=53$, which is well below $h_t=57.2\pm2.6$. Unfortunately the relatively large

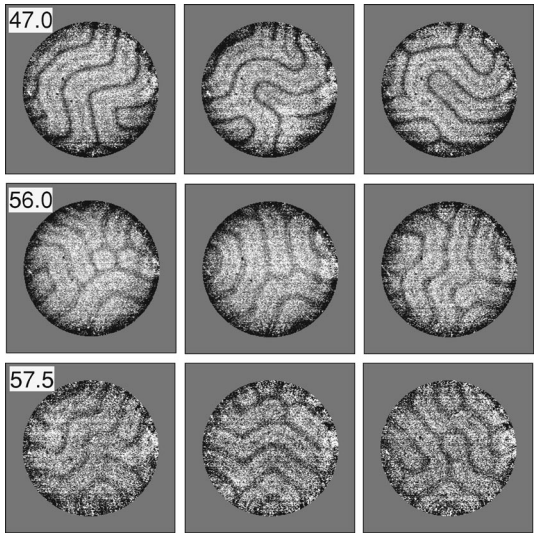

FIG. 23. Time sequences of the spatially and temporally chaotic flow for $R=4000$ and at different values of h for cell 5. The images in each row were taken at the field indicated in the leftmost image. Time increases from left to right. Images were taken in one hour intervals. The wave numbers of the patterns are $h=47$: $k_n=3.4$, $h=56$: $k_n=3.6$, $h=57.5$: $k_n=3.9$.

uncertainty of h_t and $S_{1,r}$ prevents the accurate determination of $\tilde{g}$. At h_t, we find $\tilde{g}=3/2S_{1,h}\simeq 0.3$. With increasing h, $\tilde{g}$ also increases. For instance, the data in Fig. 20 suggest that $\tilde{g}=3/2S_{1,h}-1/2S_{1,r}\simeq 0.8$ for $h=66$.

The experimental results for $1/S_{1,h}$ cannot agree quantitatively with the theory because we already know that $h_t^{\rm th}$ is lower than the experimental value. Nevertheless we calculated $1/S_{1,h}$, and give it in Fig. 20 as the dash-dotted line. We see that the relationship between $1/S_{1,h}$ and $1/S_{1,r}$ is quite similar in theory and experiment.

E. The high-field limit of R_c and k_c

It is highly probable that there exists a high-field regime where the convection phenomena become independent of the field since the director is then frozen in the homeotropic configuration. It is instructive to examine whether the experimental data extend to sufficiently high fields to fully reveal this behavior. Building on the results of FDPK [10], one can show that in a one-mode approximation the neutral curve in the limit $h\to\infty$ is given by

$$R_{c,\infty}(k)=\frac{(\lambda_\perp/\lambda_\parallel)k^2+\pi^2}{2k^2I_1^2}\left[-I_2k^2\left(\frac{2\eta_1}{\alpha_4}+\frac{2\eta_2}{\alpha_4}+\frac{2\alpha_1}{\alpha_4}\right)+k^4\frac{2\eta_2}{\alpha_4}+b^4\frac{2\eta_1}{\alpha_4}\right]. \tag{13}$$

Here $\eta_1=(\alpha_4+\alpha_5-\alpha_2)/2$ and $\eta_2=(\alpha_3+\alpha_4+\alpha_6)/2$ are Miesowicz viscosity coefficients [4], and $I_1=0.697\,38$, $I_2=-12.3026$, and $b=1.5056\pi$. This leads to $R_{c,\infty}(k_c)=3090.6$ and $k_{c,\infty}=4.294$. Using many modes, one obtains numerically $R_{c,\infty}(k_c)=3056.6$ and $k_{c,\infty}=4.328$, close to the one-mode result. One can see that only the viscosities enter into $R_{c,\infty}$, and not the elastic constants. This is so because the director is held rigid by the field. $R_{c,\infty}$ is larger than the isotropic-fluid value because of the additional viscous interaction between the flow and the rigid director field.

In the high-field limit, we obtain

$$R_c=R_{c,\infty}+R_1/h^2+O(h^{-4}). \tag{14}$$

The coefficient R_1 has not been calculated in detail, but is proportional to k_{33}^{-1}. The fact that at order $1/h^2$ elastic constants enter suggests the beginning of some director distortion by the flow.

In Figs. 21 and 22 we show the experimental data and theoretical results as a function of h^{-2}. The one-mode high-field limits $R_{c,\infty}$ and $k_{c,\infty}$ are shown in the figures as open triangles. The corresponding numerical many-mode results are given as solid triangles. The experimental data for R_c and k_c are consistent with the expected dependence on h, but respectively fall about 4% above and 1% below the calculation. The data for R_c and k_c at the highest experimental field $h\simeq 80$ are already within about 6% and 1%, respectively, of the infinite-field value. Thus it seems unlikely that qualitatively new phenomena could be discovered by measurements at even higher fields.

We examined whether the small difference between the theory and the experiment could be removed by small adjustments in the values of the fluid properties. We found that an increase by 7.5% of α_4 yielded the plusses and crosses for the data in Fig. 21 and the dashed lines in Figs. 21 and 22 (the data for k_c in Fig. 22 are not affected by changing α_4). The adjustment of α_4 produced an excellent fit for both k_c and R_c. However, it spoiled the excellent agreement for R_c along the oscillatory branch below the codimension-two point shown in Fig. 3 and did not significantly reduce the difference between calculation and experiment for k_c at small h which is shown in Fig. 9. Various other attempts to adjust the fluid properties used in the theoretical calculations were unsuccessful in yielding improved overall agreement between theory and experiment over the entire field range.

F. Nonlinear states at high fields

Beyond the codimension-two point the finite-amplitude flow was split into three regions distinguished by their characteristic wave numbers $k_n\simeq 3.4$,3.6 and 3.9. These regions are shown in Fig. 15. Figure 23 shows some characteristic patterns. Qualitatively the patterns appear similar, each exhibiting spatiotemporal chaos. The transitions between these state depended on both h and R. They were determined by measuring the change in k_n as h was varied at a given Rayleigh number. As already mentioned above, to our knowledge there are no theoretical predictions for these patterns.

ACKNOWLEDGMENTS

One of us (W.P.) acknowledges support from a NATO Collaborative Research grant. One of us (G.A.) is grateful to the Alexander von Humboldt Foundation for support. The work in Santa Barbara was supported by the National Science Foundation through Grant No. DMR94-19168.

[1] H. Bénard, Rev. Gen. Sci. Pure Appl. **11**, 1261 (1900); Ann. Chim. Phys. **23**, 62 (1901).

[2] A large literature pertaining to this field has evolved. Particularly useful as introductions to early work are the reviews by E. L. Koschmieder, Adv. Chem. Phys. **26**, 177 (1974); and in *Order and Fluctuations in Equilibrium and Nonequilibrium Statistical Mechanics*, XVIIth International Solvay Conference, edited by G. Nicolis, G. Dewel, and J. W. Turner (Wiley, New York, 1981), p. 168; and by F. Busse, in *Hydrodynamic Instabilities and the Transition to Turbulence*, edited by H. L. Swinney and J. P. Gollub (Springer, Berlin, 1981), p. 97; and in *The Fluid Mechanics of Astrophysics and Geophysics*, Vol. 4: *Mantle Convection, Plate Tectonics, and Global Dynamics*, edited by W. R. Peltier (Gordon and Breach, New York 1989).

[3] For reviews of convection in NLCs, see, for instance, E. Dubois-Violette, G. Durand, E. Guyon, P. Manneville, and P. Pieranski, in *Solid State Physics*, edited by L. Liebert (Academic, New York, 1978), Suppl. 14; and P. J. Barratt, Liq. Cryst. **4**, 223 (1989); and L. Kramer and W. Pesch, Annu. Rev. Fluid Mech. **27**, 515 (1995); and G. Ahlers, in *Pattern Formation in Liquid Crystals*, edited by L. Kramer and A. Buka (Springer, Berlin 1996).

[4] P. G. de Gennes and J. Prost, *The Physics of Liquid Crystals*, 2nd ed. (Clarendon Press, Oxford, 1993).

[5] L. M. Blinov, *Electro-Optical and Magneto-Optical Properties of Liquid Crystals* (Wiley, New York, 1983).

[6] J. Cognard, Mol. Cryst. Liq. Cryst. Suppl. Ser. **1** (1982).

[7] H. Lekkerkerker, J. Phys. (France) Lett. **38**, 277 (1977).

[8] H. Lekkerkerker, J. Phys. (Paris), Colloq. **40**, C3 (1979).

[9] E. Guyon, P. Pieranski, and J. Salan, J. Fluid Mech. **93**, 65 (1979).

[10] Q. Feng, W. Decker, W. Pesch, and L. Kramer, J. Phys. II **2**, 1303 (1992).

[11] For a summary of bifurcation types, see, for instance, Appendix A of P. Bergé, Y. Pomeau, and C. Vidal, *Order within Chaos* (Wiley, New York, 1986).

[12] D. T. J. Hurle and E. Jakeman, J. Fluid Mech. **47**, 667 (1971).

[13] For a recent review, see for instance, M. C. Cross and P. C. Hohenberg, Rev. Mod. Phys. **65**, 851 (1993).

[14] G. Ahlers, in *Pattern Formation in Liquid Crystals* (Ref. [3]).

[15] M. Velarde and I. Zúñiga, J. Phys. (Paris) **40**, 725 (1979).

[16] P. Barratt and D. Sloan, J. Fluid Mech. **102**, 389 (1981).

[17] P. Barratt and J. Manley, J. Non-Equilib. Thermodyn. **8**, 143 (1983).

[18] A. Oberbeck, Ann. Phys. Chem. **7**, 271 (1879); J. Boussinesq, *Théorie Analytique de la Chaleur*, Vol. 2. (Gauthier-Villars, Paris, 1903).

[19] F. Busse, J. Fluid Mech. **30**, 625 (1967).

[20] J. Salán and J. Fernández-Vela, Int. J. Bifurcation Chaos Appl. Sci. Eng. (to be published).

[21] E. Bodenschatz, J. de Bruyn, G. Ahlers, and D. S. Cannell, Phys. Rev. Lett. **67**, 3078 (1991).

[22] The properties were evaluated from the formulas in Appendix B of Ref. [14] for $T=25.6\,^{\circ}\mathrm{C}$ and $T_{NI}=35.17\,^{\circ}\mathrm{C}$. For the elastic constants we have $(k_{11},k_{22},k_{33})=(0.609,0.403,0.880)$ μdynes. For the Lesley viscosity coefficients we used $(\alpha_1,\alpha_2,\alpha_3,\alpha_4,\alpha_5,\alpha_6)=(-0.0718,-0.804,-0.0426,0.651,0.651,-0.19)$ dyne s/cm^2. The density was 1.022 g/cm^3, and the expansion coefficient was $\alpha=0.895\times10^{-3}$ K^{-1}. We used $(\kappa_\perp,\kappa_\parallel)=(0.677\times10^{-3},1.136\times10^{-3})$ cm^2/s and $\chi_a=1.132\times10^{-7}$ cm^3/g.

[23] G. Ahlers, D. S. Cannell, L. I. Berge, and S. Sakurai, Phys. Rev. E **49**, 545 (1994).

[24] Cell 4 was used to obtain the results reported in Ref. [14], although since that work it had been disassembled and the sample had been changed.

[25] G. Ahlers, L. I. Berge, and D. S. Cannell, Phys. Rev. Lett. **70**, 2399 (1993).

[26] We used typical fluid properties of MBBA, as cited by E. Bodenschatz, W. Zimmermann, and L. Kramer, J. Phys. (Paris) **49**, 1875 (1988), to compute the theoretical curve for R_c.

[27] G. Ahlers, in *Fluctuations, Instabilities, and Phase Transitions*, edited by T. Riste (Plenum, New York, 1974), p. 181.

[28] G. Ahlers, Phys. Rev. Lett. **33**, 1185 (1974).

[29] F. H. Busse and R. M. Clever, J. Fluid Mech. **91**, 319 (1979).

[30] C. M. Surko, P. Kolodner, A. Passner, and R. W. Walden, Physica D **23**, 220 (1986).

[31] A. Schlüter, D. Lortz, and F. Busse, J. Fluid Mech. **23**, 129 (1965).

[32] See, for instance, C. W. Meyer, G. Ahlers, and D. S. Cannell, Phys. Rev. A **44**, 2514 (1991).

[33] For small $\epsilon>0$ the unstable pure conduction state was extremely long lived because it had to evolve from spontaneous fluctuations. For $\epsilon\lesssim0.015$ its lifetime exceeded the five-hour equilibration time used in the experiment, and thus there are no data with increasing ΔT in this ϵ range. With decreasing ΔT, the decay of the amplitude to its new steady state was relatively fast and data very near $\epsilon=0$ could be taken.

[34] Tschammer, Ph.D. thesis, University of Bayreuth, Bayreuth, Germany, 1997.